Evidence of H/D Exchange within Metal-Adducted Carbohydrates after Ion/Ion-Dissociation Reactions

Darren T. Gass¹, Michael S. Cordes¹, Sebastian N. Alberti¹, H. Jamie Kim^{1#}, Elyssia S. Gallagher^{1*}

¹Department of Chemistry and Biochemistry, Baylor University, Waco, Texas 76798, USA

*Corresponding author:

Elyssia S. Gallagher

Elyssia Gallagher@baylor.edu

ORCID: 0000-0002-5411-7285

Department of Chemistry and Biochemistry, Baylor University

One Bear Place #97348, Waco, TX 76798, USA

*Current Address:

H. Jamie Kim

Laboratory of Bacterial Saccharides, Office of Vaccines Research and Review, Center for Biologics Evaluation and Research, U.S. Food and Drug Administration

10903 New Hampshire Ave, Silver Spring, MD 20903, USA

Abstract:

Tandem mass spectrometry (MS/MS) using fragmentation has become one of the most effective methods for gaining sequence and structural information of biomolecules. Ion/ion reactions are competitive reactions where either proton transfer (PT) or electron transfer (ET) can occur from interactions between multiply charged cations and singly charged anions. Utilizing ion/ion reactions with fluoranthene has offered a unique method of fragment formation for structural elucidation of biomolecules. Fluoranthene is considered an ideal anion reagent because it selectively causes electron transfer dissociation (ETD) and minimizes PT when interacting with peptides. However, limited investigations have sought to understand how fluoranthene – the primary, commercially available anion reagent – interacts with other biomolecules. Here, we apply deuterium labeling to investigate ion/ion reaction mechanisms between fluoranthene and divalent, metal-adducted carbohydrates (Ca²⁺, Mg²⁺, Co²⁺, and Ni²⁺). Deuterium labeling of carbohydrates allowed us to observe evidence of hydrogen/deuterium exchange (HDX) occurring after ion/ion dissociation reactions. The extent of deuterium loss is dependent on several factors, including the physical properties of the metal ion and the fragment structure. Based on the deuterium labeling data, we have proposed ETD, PTD, and intermolecular PT – also described as HDX - mechanisms. This research provides a fundamental perspective of ion/ion and ion/molecule reaction mechanisms and illustrates properties that impact ion/ion and ion/molecule reactions for carbohydrates. Together, this could improve the capability to distinguish complex and heterogenous biomolecules, such as carbohydrates.

1. Introduction

Gas-phase ion/ion reactions^{1, 2} have become valuable within the mass spectrometry (MS) community because they enable structural characterization of a variety of analytes, including peptides,^{3, 4} intact proteins,⁵⁻⁷ and carbohydrates.^{8, 9} Electron transfer dissociation (ETD)¹⁰ is an ion/ion reaction in which an anion reagent transfers an electron to a multiply charged, cationic analyte. During the reaction, charge reduction of the cationic analyte occurs, limiting ETD to multiply charged parent ions. ETD is the most commonly used ion/ion reaction because unique fragments can be formed, compared to collision-induced dissociation (CID),¹¹ allowing for increased and complementary fragmentation of biomolecules. Specifically, ETD can fragment protein backbones while retaining labile post-translational modifications.^{10, 12, 13} Additionally, ETD can minimize intramolecular hydrogen migration, enabling deuterium localization within labeled peptides and proteins, while CID causes significant intramolecular hydrogen migration.¹⁴⁻¹⁶ The unique fragmentation properties of ETD compared to CID are hypothesized to result from differences in fragmentation mechanisms.^{10, 17}

In ion/ion reactions, the anion reagent influences the reaction products. Though several anions have been effective as ETD reagents for fragmentation of peptides and proteins, ¹⁸⁻²⁰ fluoranthene efficiently transfers an electron to most biomolecules ¹⁸ and will be the focus here. When fluoranthene interacts with peptides and proteins, electron transfer (ET) has been proposed to compete with proton transfer (PT). ¹⁸ However, fluoranthene is not a common PT reagent because many other anion reagents maximize PT. ¹⁸ Recent data from the Hunt lab has indicated that some reagents enable both PT and ET in a stepwise manner with a single anion. ²¹ The primary purpose of PT with biomolecules has been to reduce the charge of ions to improve the resolution of fragments or intact species in mass spectra ^{6,7,22,23} with PT rarely causing dissociation, except for glycosaminoglycans ²⁴ and oligonucleotides. ²⁵

The Jørgensen group proposed that intermolecular PT could occur between fluoranthene and a multiply protonated peptide. ¹⁴ This intermolecular PT could induce the loss of labile hydrogens as they are replaced with hydrogens from the anion reagent. Unlike an initial PT reaction, intermolecular PT does

not change the charge of the ion. Therefore, intermolecular PT, which is a form of gas-phase hydrogen/deuterium exchange (HDX), can only be detected when using either deuterated analytes or reagent anions, resulting in mass differences between the hydrogen atoms in the cation and reagent anion. Intermolecular PT could occur from either an anion reacting with a fragment via an ion/ion reaction or by a neutral fluoranthene interacting with a fragment in an ion/molecule reaction. However, deuterium-labeling data suggested that this proposed intermolecular PT was minimal for protonated peptides after dissociation from reactions with fluoranthene.¹⁴

Glycans are biologically relevant carbohydrates and critical post-translational modifications that change protein and lipid function based on their structures. ²⁶⁻²⁸ Carbohydrates are challenging to analyze because of the naturally abundant linkage, anomeric, and compositional isomers within biological systems. ²⁹⁻³¹ Mass spectrometry (MS) has become a valuable method for analyzing carbohydrates; ³²⁻³⁵ however, tandem MS (MS/MS) methods are necessary to distinguish isomeric species. Because isomers have the same mass-to-charge ratio (*m/z*), fragmentation methods can be used to create unique fragments based on the structure of the precursor ion. One promising MS/MS method for differentiating isomeric carbohydrates has involved using ion/ion reactions to induce fragmentation. ^{8, 9} Ion/ion reactions using fluoranthene have resulted in formation of unique carbohydrate fragments that are not seen with other fragmentation methods, such as CID.

Table 1. Physical properties of metal ions.

	Charge Density	Second-Ionization Energy	Electron
Metal	$(1.6 \times 10^{-19} \text{C/nm}^3)$	(kJ/mol)	Configuration
Ca ²⁺	1350	1150	[Ar]
Mg^{2+}	3140	1450	[Ne]
Co ²⁺	2890	1650	$[Ar]3d^7$
Ni ²⁺	3500	1750	[Ar]3d ⁸

Divalent metal ions, such as Ca²⁺, Mg²⁺, Co²⁺, or Ni²⁺, adduct to carbohydrates and form doubly charged gas-phase ions,³⁶ which are necessary for ion/ion reactions due to the charge reduction. The fragments formed, including the extent of cross-ring cleavages, from ion/ion reactions with fluoranthene

are affected by the identity and properties of the metal adducted to the carbohydrate.^{8, 35} Table 1 shows the physical properties of the metals investigated here, including the charge density,³⁷ second-ionization energy,³⁸ and electron configuration.

Here, we investigate the dissociation mechanism of ion/ion reactions between fluoranthene and metal-adducted carbohydrates. Carbohydrates are structurally unique compared to peptides and readily ionize by metal adduction rather than protonation during ESI, making the charge carrier distinct between these biomolecules. ^{39, 40} We use deuterium labeling to monitor the labile hydrogens of metal-adducted carbohydrates during and after ion/ion dissociation reactions with fluoranthene. We detect unique extents of deuterium loss based on the metal-charge carrier. Based on this data, we hypothesize that specific physical properties of the metal-charge carriers correlate to the fragments formed and the extent of HDX. We propose ETD, PTD, and intermolecular PT mechanisms to explain the deuterium labeling data. To our knowledge, this is the first report of HDX for metal-adducted carbohydrate fragments after ion/ion dissociation reactions with fluoranthene. These studies are significant in providing a fundamental understanding of ion/ion reaction mechanisms, specifically between fluoranthene and metal-adducted carbohydrates, which will continue to provide insight to analyzing carbohydrate isomers.

2. Methods

a. Materials

Melezitose (Glc(α1-3)Fru(β2-1α)Glc) was from Sigma Aldrich (St. Louis, MO). Calcium acetate and magnesium chloride were from VWR (Radnor, PA). Cobalt chloride, nickel chloride, methanol, and deuterated methanol (99.0%) were purchased from Fisher Scientific (Waltham, MA). All chemicals were used without further purification. Nanopure water was obtained from a Purelab Flex 3 purification system (Elga, Veolia Environment S. A., Paris, France).

b. Sample preparation for deuterium experiments

Sample storage containers (1.5 mL, polypropylene) were cleaned with two 1-mL washes of nanopure water and two 1-mL washes of methanol and dried prior to use. Melezitose was mixed with each metal salt at 25 μM: 50 μM ratio (carbohydrate: metal salt) in either protonated (99.25: 0.75 (v/v) methanol: nanopure water) or deuterated (92.5: 6.75: 0.75 (v/v/v) deuterated methanol: methanol: water) solvent as described in previous protocols.^{41, 42} Samples were stored at 0 °C for 18-24 hours to allow complete deuterium labeling of labile protons in melezitose.

c. Mass spectrometry

All experiments used an Orbitrap Fusion Tribrid MS (Thermo-Fisher Scientific, Waltham, MA)⁴³ equipped with an EASY-Max NG ion source.⁴⁴ Experiments employed spray voltage: 3.5 kV, capillary temperature: 120 °C, vaporizer temperature: 75 °C, RF Lens: 60%, and infusion flow rate: 5-8 μL/min. Aux gas: N₂, 5-11 arb units, sheath gas: N₂, 1-4 arb units, and sweep gas: N₂, 1-2 arb units were optimized daily to maximize the precursor ion signal (~5.0x10⁶ to 4.0x10⁷). Spectra were recorded as an average of 30 scans using a resolving power of 240,000 and a mass range from 150-700 *m/z*. To clean the ESI needle of residual salts and minimize metal carryover between experiments, ~200 μL of nanopure water was injected before and after use of each metal salt. Samples were injected for ~8 to 10 minutes before recording data for each trial to equilibrate the environment around the ESI source, ⁴⁵ improving deuterium uptake and preventing sample carryover from previous trials.

Ion/ion reactions were performed with fluoranthene as the anion reagent for reaction times between 50 ms and 150 ms. At reaction times longer than 150 ms, signal loss for fragments occurred due to significant neutralization. Fluoranthene signal target was set to 2.0×10^5 . The fully deuterated and undeuterated precursor ions were isolated with a $0.5 \, m/z$ or $10.0 \, m/z$ isolation width.

To monitor the formation of fragments from quadrupole isolation and HDX after collision-induced dissociation, control experiments were run using higher-energy collisional dissociation (HCD) because the software prevented 0 ms ion/ion reaction times. The fully deuterated and undeuterated precursor ions were isolated with isolation widths from $0.5 \, m/z$ to $20.0 \, m/z$. HCD was used at 0% normalized collision

energy (NCE). The pressure in the HCD cell was \sim 0.008 torr. All other experimental settings were the same as described above.

Experiments were run to examine if HDX could occur from interactions with fluoranthene. Fragments were formed by in-source activation using the conditions described above and then isolated using isolation widths of $10.0 \, m/z$. The fragments were trapped in the presence or absence of fluoranthene using fluoranthene signal targets of 2.0×10^5 or 1.0, respectively. Trapping/reaction times were 50 ms or 150 ms. All other parameters were the same as described above.

d. Data processing

Melezitose is a nonreducing sugar; therefore, isotopic labeling could not be used to distinguish the isomeric reducing/non-reducing ends. Fragment labels include all possible isomers from both ends of melezitose according to the Domon and Costello fragmentation nomenclature.⁴⁷ For example, a fragment label could be $[^{1.4}X_2/A_3, ^{0.3}X_2/A_3 + C_2/Y_2 + Ca - H]^+$. The slash between $^{1.4}X_2$ and $^{1.4}A_3$ displays the isomeric fragments from both ends of the carbohydrate. The comma in the fragment label shows that the isomeric fragments are isomeric. The addition sign between the X/A and C/Y fragments means that this fragment is an internal cleavage that losses a fragment on both the reducing and nonreducing end. For example, the $^{1.4}X_2$ cross-ring cleavage could be combined with a C_2 glycosidic bond cleavage. Fragments were identified manually by computing theoretical m/z values with the assistance of Glycoworkbench⁴⁸ and Chemdraw 21.0. The signal-to-noise (S/N) was calculated by Thermo Scientific FreeStyle (ver 1.6). All identified, undeuterated fragments and precursors had a mass error tolerance of ± 10.00 ppm and a S/N ≥ 10.00 . All deuterium-labeled fragments and precursors had a mass error tolerance of ± 10.50 ppm and a S/N ≥ 3.00 .

Eq. 1 was used to calculate the weighted-average masses (M) of fully deuterated and undeuterated metal-adducted carbohydrates. This calculation requires experimentally determined m/z and intensities (I) for each peak.

$$M = \frac{(\Sigma \frac{m}{z} I)}{\Sigma I} \quad (1)$$

In Eq. 2, the maximum deuterium uptake (D_{max}) was calculated by finding the weighted-average m/z for the fully deuterated parent or fragment ion, subtracting the weighted-average m/z for the undeuterated parent or fragment ion, multiplying this difference by the charge (z), and dividing by the mass difference between deuterium and hydrogen (1.00627 Da).⁴⁹

$$D_{max} = Z \cdot \frac{M_{deuterated} - M_{undeuterated}}{1.00627}$$
 (2)

For experiments with quadrupole isolation widths greater than $0.5 \, m/z$, a correction factor (CF) was used to calculate the contribution of the fully deuterated precursor to the detected D_{max} value. A CF is unnecessary when using an isolation width of $0.5 \, m/z$ because the fully deuterated melezitose was isolated with no detected deuterium loss for the isolated precursor ion before or after the ion/ion reaction (CF = 1). When using an isolation width larger than $0.5 \, m/z$, we isolated partially back-exchanged melezitose that had less than 11 deuteriums. A CF is necessary to compare data collected using different isolation widths. CF (Eq. 3) is calculated by determining the number of labile hydrogens in the analyte that could exchange with deuterium and dividing this value by the experimental D_{max} (Eq. 2) of the ion.

$$CF = \frac{\text{# of labile hydrogens}}{precursor D_{max}} (3)$$

The corrected D_{max} (Eq 4.) is determined by multiplying the CF (Eq. 3) by the D_{max} (Eq. 2).

corrected
$$D_{max} = CF \cdot D_{max}$$
 (4)

Data is presented as the average \pm standard deviation for a minimum of four replicate trials. For comparisons of D_{max} values, a Student's or Welch's t-test was used based on the results of an F-test at the 95% or 99% confidence intervals.

e. Molecular Dynamics Simulations

Initial structures of melezitose were generated with the carbohydrate builder, GLYCAM-Web⁵⁰ and optimized by density functional theory (DFT) using Gaussian 16⁵¹ at the B3LYP-6311++ G(d,p) level of theory. Molecular dynamics (MD) simulations were modeled in GROMACS/2018.3⁵² using the CHARMM36 forcefield⁵³ with molecular topologies of the optimized melezitose being generated with the CGenFF-4.0 server.⁵⁴ The MD methodology adopted for simulating ESI of carbohydrates is based on protocols described by the Konermann^{55, 56} and Gallagher³⁹ groups. To model ESI droplets, a single melezitose was inserted into a droplet with a 2.5 nm radius of TIP4P/2005⁵⁷ water along with seven ions, either Ca²⁺, Mg²⁺, Co²⁺, or Ni²⁺, corresponding to a droplet charge just below the Rayleigh limit. To model vacuum conditions, the droplet was simulated in a 999 nm³ box with maximum allowable values for non-bonded force cutoffs to enable the use of GPU acceleration with periodic boundary conditions.⁵⁵ The droplet was energy minimized and NVT/NPT equilibrated prior to production MD runs. The MD simulation was run at 370 K for 25 ns and 425 K for 15 ns to model in-source temperature with evaporated waters being deleted every 0.25 ns, resulting in complete droplet desolvation and carbohydrate-metal ion adduct formation. One hundred post-ESI structures of melezitose-metal adducts were optimized using DFT. The optimized structures were assessed with an in-house python script to calculate interatomic distances between the glycosidic oxygens and hydrogens on the terminal monosaccharides to determine the likelihood of specific disassociation mechanisms.

3. Results and Discussion

a. Metal ions influence fragment formation

We examined ion/ion reactions between fluoranthene and melezitose adducted to Ca²⁺, Ni²⁺, Co²⁺, or Mg²⁺. We specifically selected Ca²⁺ and Mg²⁺ because these metals are known to improve ionization efficiencies for metal-adducted carbohydrate ions.^{8, 36} Ni²⁺ and Co²⁺ were selected because previous results showed higher fragmentation efficiency and formation of additional cross-ring cleavages compared with Mg²⁺- and Ca²⁺-adducted tetrasaccharides.⁸ These four metal ions have distinct physical

properties (Table 1), including charge density, second-ionization energy, and electron configuration, which have been hypothesized to impact fragmentation of metal-adducted carbohydrates.⁸ Specifically, higher charge-density metal ions have been seen to increase the number of energetically favorable fragmentation pathways for metal-adducted carbohydrates during ETD. Metals with a higher second-ionization energy increase the interactions between the metal and lone pair electrons on oxygen atoms.³⁶, This is hypothesized to lead to an increase in the number of fragmentation pathways and the fragmentation efficiency when comparing Mg²⁺- and Ca²⁺-adducted carbohydrates to Ni²⁺- and Co²⁺-adducted carbohydrates. Finally, the electron configurations of Ni²⁺ and Co²⁺ contain d-orbitals that are neither half empty nor full, which is hypothesized to lead to an increase in fragmentation pathways compared with Mg²⁺- and Ca²⁺-adducted carbohydrates.⁸

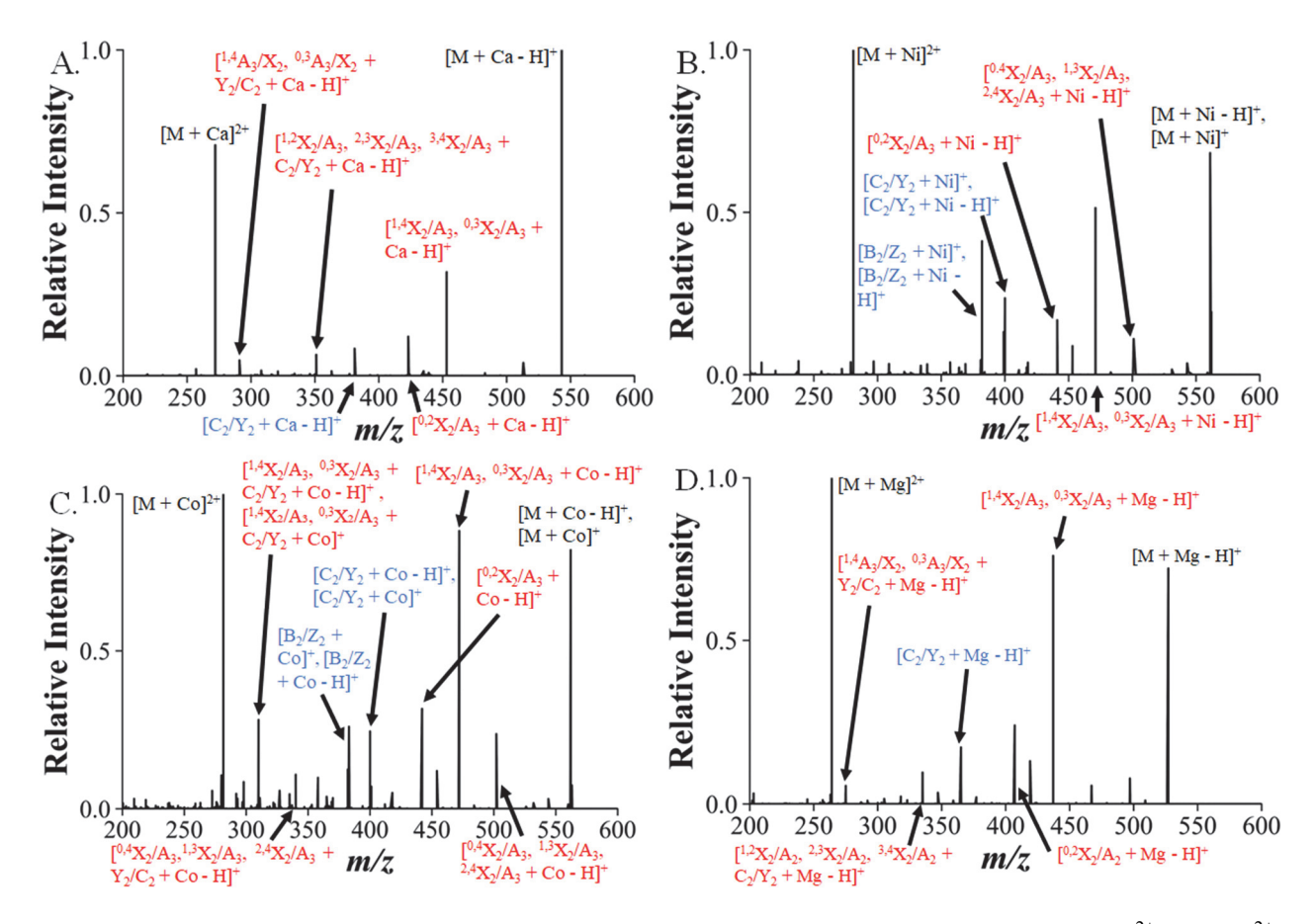


Figure 1. Representative ion/ion reaction spectra using an isolation width of 0.5 *m/z* for (A) Ca²⁺-, (B) Ni²⁺-, (C) Co²⁺-, and (D) Mg²⁺-adducted melezitose (M) reacted with fluoranthene for 50 ms. The precursor and neutral-loss fragments are labeled in black, glycosidic-bond cleavages are labeled in blue, and cross-ring or internal cleavages are labeled in red. For fragments produced from the same bond cleavage/cleavages (e.g., charge reduced and hydrogen loss), the neighboring peaks are labeled with the higher intensity fragment listed first.

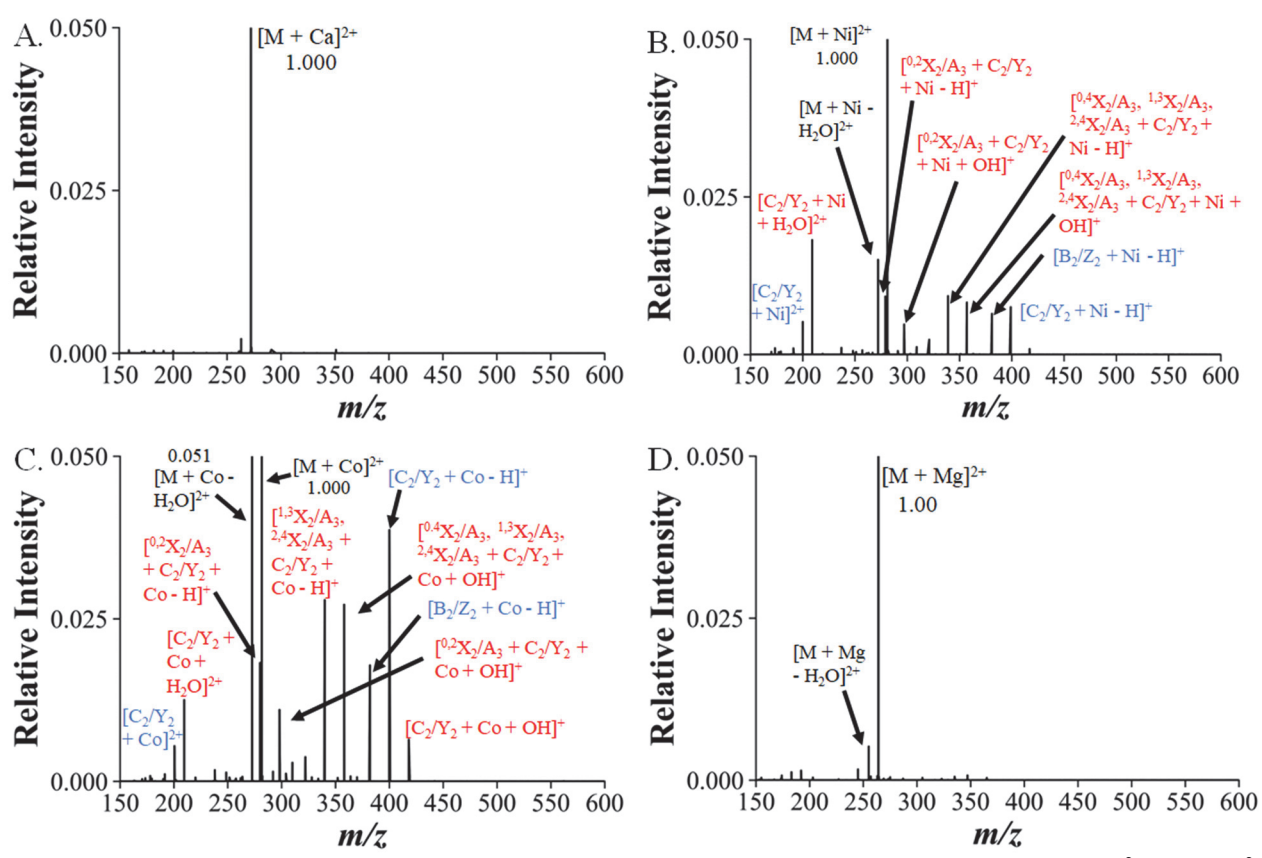
We first investigated the ion/ion reaction spectra (50 ms reaction with fluoranthene) for undeuterated, metal-adducted melezitose to identify fragments that were formed from all four metal-ion adducts. Figure 1 shows that the fragment intensities varied based on the metal-charge carrier. Similar to previous results, Co²⁺-adduction provided the most unique fragments compared with the other three metals.⁸ We only detected fragments; complexes of fluoranthene attached to either metal-adducted melezitose ions or fragment ions were not detected following the ion/ion reactions. Labeled fragments in Figure 1 are detected for all four metal adducts and examined below following deuterium labeling. Complete tables of all identified fragments can be found in the Supporting Information, Tables S1-S4.

We expected to see predominantly charge-reduced fragments for all metal adducts, of the form [fragment + metal]⁺, based on previous results.⁸ However, the data primarily showed fragments with hydrogen loss, as [fragment + metal - H]⁺, for all metal adducts (Figure 1, Tables S1-S4). Charge-reduced fragments were detected for every metal adduct, though Ni²⁺- and Co²⁺-adducted melezitose formed the most charge-reduced fragments (Tables S1-S4). The charge-reduced fragments tended to form from glycosidic-bond cleavages ([C₂/Y₂ + metal]⁺ or [B₂/Z₂ + metal]⁺) at much higher intensities compared to cross-ring cleavages ([^{1,4}X₂/A₃, ^{0,3}X₂/A₃ + metal]⁺ or [^{0,2}X₂/A₃ + metal]⁺) (Figures 1B and 1C). This is important because charge reduction indicates that ET occurred, while hydrogen loss can occur from either ET or PT.^{59,60} These results are similar to previous studies that primarily observed hydrogen loss for fragments formed following electron-capture dissociation (ECD)⁶¹ of divalent metal-adducted carbohydrates.^{58,62} Based on the data, we hypothesize that Ni²⁺ and Co²⁺ have unique metal-ion properties that result in distinct ion/ion reaction mechanisms compared with Mg²⁺ and Ca²⁺. The higher second-ionization energy and electron configurations of Ni²⁺ and Co²⁺ compared with Mg²⁺ and Ca²⁺ (Table 1) could allow for the formation of more charge-reduced fragments, implying that additional mechanistic differences for the ion/ion reactions occur with fluoranthene based on the metal adduct.

In the ion/ion reaction spectra, we identified doubly charged fragments for every metal adducted to melezitose (Tables S1-S4), suggesting that fragmentation from collisional activation also occurred. Because we detected doubly charged fragments, we ran additional experiments (Figure 2) to determine the fragments formed during quadrupole isolation, which has been known to cause dissociation of other biomolecules. 63, 64

We saw distinct differences in the quadrupole-isolation induced collisional-activation spectra based on the metal adduct (Figure 2). With Ca²⁺-adducted melezitose, the fewest fragments were identified (Table S5), with none above a relative intensity of 0.005 (Figure 2A). More fragments were detected with Co²⁺ and Ni²⁺ compared with Ca²⁺ and Mg²⁺ (Figure 2 and Tables S5-S8). The number and relative intensity of the fragments increases as the second-ionization energy of the metal increases (Table 1). We

propose that metals with electron configurations with unfilled d-orbitals and higher second-ionization energies form less stable metal-adducted carbohydrate ions during ESI, causing facile dissociation during quadrupole isolation. In comparison, the charge density is likely less significant in regard to ion stability because the high charge densities of both Mg²⁺ and Ni²⁺ lead to different quadrupole-dissociation results. With an isolation width of 0.5 m/z, 53 of the 65 total fragments formed from quadrupole-isolation induced dissociation for all four metal-ion adducts were also detected from the ion/ion reactions. Thus, ~23% of the doubly and singly charged fragments detected after the ion/ion reaction were formed from collisional activation in the quadrupole (Tables S1-S8). Additionally, 11 fragments detected following quadrupole-isolation induced dissociation are doubly charged ions that were not detected following ion/ion reactions, which could indicate that these doubly charged ions could be further fragmented during the ion/ion reaction and detected as singly charged fragments.



Figures 2. Representative quadrupole-isolation induced collisional-activation spectra for (A) Ca^{2+} -, (B) Ni^{2+} -, (C) Co^{2+} -, and (D) Mg^{2+} -adducted melezitose (M) using an isolation width of 0.5 m/z. Fragment colors and labels are the same as Figure 1.

Increasing the isolation width can minimize fragmentation of non-stable ions by decreasing the kinetic energy applied to the ions moving through the quadrupole. The decrease in kinetic energy lowers the probability of collisions with other ions or neutrals during movement through the quadrupole, which minimizes the transfer of vibrational energy to the ion and dissociation. We investigated changing the isolation width with Co^{2+} -adducted melezitose because we observed the largest extent of fragmentation during quadrupole isolation for this metal-adducted carbohydrate (Figure 2C). The number of identifiable fragments from collisional activation of Co^{2+} -adducted melezitose decreased as the isolation width increased from 0.5 m/z to 20.0 m/z (Tables S7, S9 – S12). Therefore, we used isolation widths of 0.5 m/z and 10.0 m/z for all additional experiments.

b. HDX is metal-charge carrier dependent

We then fragmented metal-adducted melezitose following deuterium labeling to determine if ion/ion reactions predominantly yielded fragmentation products with minimal HDX, as previously seen for protonated peptides. Here, we used isolation widths of 0.5 *m/z* with the goal to isolate only the fully deuterated precursor (Figures 3A, 3D, and S1), which allowed us to predict the number of deuterium labels on each fragment based on ECD mechanisms proposed by the Costello group.⁶⁵ We used proposed ECD mechanisms because the initial electron capture/electron transfer steps leading to dissociation have been hypothesized to be mechanistically similar.⁶⁶

Ni²⁺ and Mg²⁺ have multiple isotopic masses, which adds complexity to the mass spectra when examining deuterium-labeled melezitose. For Ni²⁺- and Mg²⁺-adducted melezitose, the most intense precursor peaks are associated with the ⁵⁸Ni²⁺ and ²⁴Mg²⁺ isotopes, respectively. Lower intensity peaks exist for the ⁶⁰Ni²⁺, ²⁵Mg²⁺, and ²⁶Mg²⁺ isotopes. Thus, partially back-exchanged precursors ([M + ⁶⁰Ni²⁺ + 9D]²⁺, [M + ²⁵Mg²⁺ + 10D]²⁺, [M + ²⁶Mg²⁺ + 9D]²⁺) can be isolated with the fully labeled precursors ([M + ⁵⁸Ni²⁺ + 11D]²⁺, [M + ²⁴Mg²⁺ + 11D]²⁺) when using an isolation width of 0.5 m/z. Ca²⁺ and Co²⁺ only have one predominant isotope (>95%), ⁴⁰Ca²⁺ and ⁵⁹Co²⁺, simplifying the spectra for the isolated precursors compared to Ni²⁺ and Mg²⁺. However, when calculating D_{max}, we use a mass-error selection criteria of 10.5 ppm. The m/z of ⁶⁰Ni²⁺-, ²⁵Mg²⁺-, and ²⁶Mg²⁺-adducted precursors and fragments are above the 10.5 ppm mass-error threshold when calculating D_{max} for the ⁵⁸Ni²⁺ and ²⁴Mg²⁺ peaks, leading to their exclusion from the D_{max} calculations. Thus, the high mass accuracy of the Orbitrap Fusion allowed us to selectively monitor the fragments resulting only from the fully deuterated precursors, even though additional ions were isolated using an isolation width of 0.5 m/z.

We initially focused on deuterium labeling for the C_2/Y_2 fragments because these fragments were detected with all four metals at high relative intensities (Figure 1). For the C_2/Y_2 fragment adducted to Ni^{2+} , we expected to see seven or eight deuterium labels (Figure 3B) because we detected both the $[C_2/Y_2 + Ni - H]^+$ and $[C_2/Y_2 + Ni]^+$ fragment, at 399.0412 m/z and 400.0490 m/z, respectively. With the Ni^{2+} -adducted C_2/Y_2 fragments, we detected between three and eight deuterium labels, though the most intense peak had eight deuterium (Figure 3C). For the Ca^{2+} -adducted C_2/Y_2 fragments, we expected to detect seven deuterium labels on the fully deuterated fragments because we only identified fragments with hydrogen loss ($[C_2/Y_2 + Ca - H]^+$) at 381.0687 m/z (Figure 3E). The data, however, showed a distribution with the fragments having between one and seven deuterium at a reaction time of 50 ms with the most

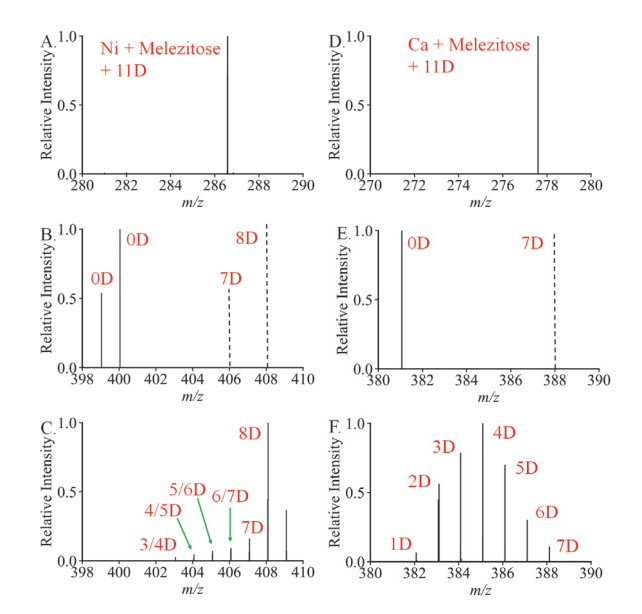


Figure 3. Representative spectra for (A) Ni^{2+} and (D) Ca^{2+} -adducted, fully deuterated precursors; (B) Ni^{2+} and (E) Ca^{2+} -adducted, undeuterated C_2/Y_2 fragments (solid) and theoretical, fully deuterated C_2/Y_2 fragments (dashed); and (C) Ni^{2+} and (F) Ca^{2+} -adducted C_2/Y_2 fragments after ion/ion reactions (50 ms). All isolation widths were $0.5 \, m/z$. D represents the number of deuterium in the fragments. For Ni^{2+} , the first and second number represent deuterium for the charge-reduced ($[C_2/Y_2 + Ni]^+$) and hydrogen loss ($[C_2/Y_2 + Ni - H]^+$) fragments, respectively. Unlabeled peaks in the spectra were excluded from the D_{max} calculations due to the m/z values being outside the mass-error threshold.

intense peak containing four deuterium (Figure 3F). Only \sim 3% of Ca²⁺-adducted C₂/Y₂ fragment ions retained the expected seven deuterium, indicating that \sim 97% of the Ca²⁺-adducted C₂/Y₂ fragments underwent HDX. HDX was also detected for the C₂/Y₂ fragments adducted to Mg²⁺ and Co²⁺ (Figure S1), with a trend of Ca²⁺> Mg²⁺>Co²⁺>Ni²⁺ for the most HDX to the least HDX.

c. Reaction time and fragment identity alter the extent of HDX

The reaction time for ion/ion reactions alters the intensity of the detected fragments; 46 therefore, we examined how changing the ion/ion reaction time altered HDX. We hypothesized that longer reaction times would increase the potential for interactions with fragments, leading to more HDX. Figure 4 shows the D_{max} for the Ni^{2+} , Co^{2+} , Mg^{2+} , and Ca^{2+} -adducted C_2/Y_2 fragments at increasing reaction times. We detected a difference in the D_{max} values between reaction times of 50 ms and 150 ms for C_2/Y_2 fragments adducted to Ni^{2+} , Co^{2+} , and Ca^{2+} (Table S13). For example, the D_{max} of the Ca^{2+} -adducted C_2/Y_2 fragments changed from (3.86 \pm 0.09) D to (3.08 \pm 0.09) D at reaction times of 50 ms and 150 ms, respectively (Figure 4). The change in D_{max} for Ca^{2+} -adducted C_2/Y_2 fragments can also be seen in the deuterium distributions as the peak with maximum intensity shifted from four deuterium at a reaction time of 50 ms to three deuterium at a reaction time of 150 ms (Figures 3B and S2). This data indicates that more HDX can occur at longer reaction times for certain metal-ion adducts.

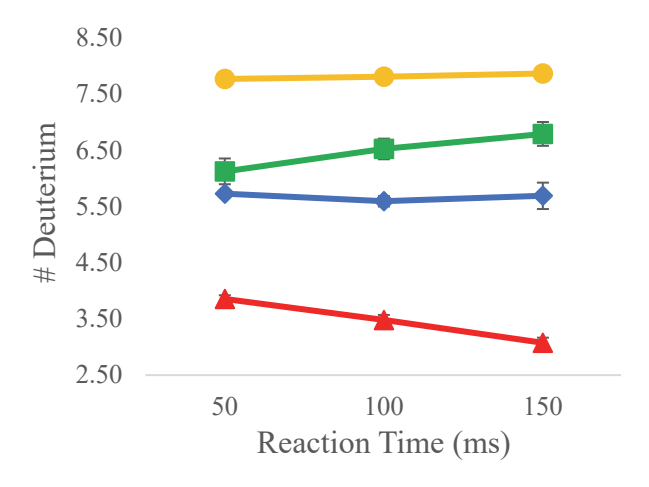


Figure 4. D_{max} values for the metal-adducted C_2/Y_2 fragments formed by ion/ion reactions with fluoranthene at multiple reaction times $(0.5 \ m/z)$ isolation width). D_{max} for $[C_2/Y_2 + Ni]^+/[C_2/Y_2 + Ni - H]^+$ are shown as yellow circles, $[C_2/Y_2 + Co - H]^+/[C_2/Y_2 + Co]^+$ are green squares, $[C_2/Y_2 + Mg - H]^+$ are blue diamonds, and $[C_2/Y_2 + Ca - H]^+$ are red triangles. Data points represent the average D_{max} with error bars showing the standard deviation (n=12).

Figure 4 shows that the change in D_{max} is also dependent on the metal-charge carrier. The D_{max} decreased by 0.78 D for the Ca^{2+} -adducted C_2/Y_2 fragments and increased by 0.10 D and 0.7 D for the Ni^{2+} - and Co^{2+} -adducted C_2/Y_2 fragments, respectively, when comparing the D_{max} after reaction times of 50 ms and 150 ms. The D_{max} for Mg^{2+} -adducted C_2/Y_2 fragments was within experimental error when comparing reaction times of 50 ms and 150 ms. The increase in D_{max} at longer reaction times was unique to Co^{2+} - and Ni^{2+} -adducted C_2/Y_2 and B_2/Z_2 fragments (Table S13). Formation of the Co^{2+} - and Ni^{2+} -adducted C_2/Y_2 fragments can occur from both quadrupole isolation and interactions with fluoranthene (Figure 2, Tables S7- S8); therefore, the effects of quadrupole isolation on HDX are examined in more detail below (Figure 5). Yet, this data shows that both the reaction time and metal adduct are important for HDX.

We examined the extent of HDX for the precursor ions that remain after ion/ion reactions. For all metals, the fully deuterated melezitose that remained after 150 ms of reaction showed no detectable HDX, maintaining 11 deuterium labels (Table 2, S13). This difference in HDX for the precursor ions compared to the C₂/Y₂ fragments (Figure 3) suggests that the HDX that we are observing occurs after ETD or PTD. Thus, the structures of the fragment ions appear to play a role in the magnitude of HDX that is observed.

We examined HDX in different fragments (Table 2). We first examined the D_{max} of Ca^{2+} -adducted fragments because we saw the most extensive HDX with Ca^{2+} -adducted C_2/Y_2 fragments. The D_{max} for the $[^{1,4}X_2/A_3, ^{0,3}X_2/A_3 + Ca - H]^+$ and $[^{1,4}X_2/A_3, ^{0,3}X_2/A_3 + C_2/Y_2 + Ca - H]^+$ fragments display less HDX compared with the other four fragments adducted to Ca^{2+} (Table 2). For example, for the $[^{1,4}X_2/A_3, ^{0,3}X_2/A_3 + Ca - H]^+$ fragments, we expected a D_{max} of seven or eight deuterium from the proposed structures of the fragments (Figure S3). Table 2 shows that $[^{1,4}X_2/A_3, ^{0,3}X_2/A_3 + Ca - H]^+$ had a D_{max} of (6.76 ± 0.07) D at a reaction time of 150 ms. The D_{max} for $[^{1,4}X_2/A_3, ^{0,3}X_2/A_3 + Ca - H]^+$ is ~ 10 % below the expected D_{max} , whereas the D_{max} for $[C_2/Y_2 + Ca - H]^+$ is ~ 56 % below the expected D_{max} at a reaction time of 150 ms. This indicates that HDX for Ca^{2+} -adducted fragments is also dependent on the fragment.

Table 2. D_{max} for Ca^{2+} -adducted fragments and remaining precursor ions identified in Figure 1A from ion/ion reactions with fluoranthene at multiple reaction times using an isolation width of 0.5 m/z.

	Theoretical			
Fragment/Precursor	$\mathrm{D_{max}}^a$	50 ms D _{max} ^b	$100 \text{ ms } D_{\text{max}}^{b}$	$150 \text{ ms } D_{\text{max}}^{b}$
$[M + Ca]^{2+}$	11.00	10.9990 ± 0.0003	10.9997 ± 0.0002	11.0000 ± 0.0002
$[C_2/Y_2 + Ca - H]^+$	7.00	3.86 ± 0.07	3.48 ± 0.09	3.08 ± 0.09
$[M + Ca - H]^+$	10.00	5.70 ± 0.03	5.13 ± 0.06	4.69 ± 0.06
$\left[{}^{1,4}X_{2}/A_{3}, {}^{0,3}X_{2}/A_{3} + C_{2}/Y_{2} + \right]$	5.00	4.70 ± 0.03	4.66 ± 0.03	4.69 ± 0.07
Ca - H] ⁺				
$[^{1,2}X_2/A_3, ^{2,3}X_2/A_3, ^{3,4}X_2/A_3]$	7.00	4.22 ± 0.08	3.83 ± 0.06	3.4 ± 0.2
$+ C_2/Y_2 + Ca - H]^+$				
$[^{0.2}X_2/A_3 + Ca - H]^+$	7.00	4.0 ± 0.2	3.7 ± 0.2	3.3 ± 0.3
$[^{1,4}X_2/A_3,^{0,3}X_2/A_3 + Ca - H]^+$	7.00/8.00	7.01 ± 0.02	6.87 ± 0.03	6.76 ± 0.07

 $^{^{}a}$ Different theoretical D_{max} exist for isomeric fragments, which are listed based on the fragment order.

^b Data represents the average \pm standard deviation (n=12).

We then compared HDX in fragments adducted to the other metals to examine the dual effects of the charge carrier and the fragment structure (Tables 2-3 and S13). Minimal HDX was observed for the Ni²⁺-, Co²⁺-, and Mg²⁺-adducted [$^{1,4}X_2/A_3$, $^{0,3}X_2/A_3$ + metal - H]⁺ fragments, similar to the trend observed for Ca²⁺-adducted fragments. The D_{max} value for all examined fragments followed the trend observed for the C₂/Y₂ fragments with Ca²⁺<Mg²⁺ \leq Co²⁺ \leq Ni²⁺ (Table S13). Although, there were some cases where the D_{max} for a Mg²⁺-adducted fragment was higher than the D_{max} for the same Co²⁺-adducted fragment, as seen with the [$^{1,4}X_2/A_3$, $^{0,3}X_2/A_3$ + metal - H]⁺ fragments (Table 3). The data here suggests that specific interactions occur for each fragment and charge carrier, resulting in different amounts of HDX.

Table 3. D_{max} for Ni²⁺-, Mg²⁺-, and Co²⁺-adducted [$^{1,4}X_2/A_3$, $^{0,3}X_2/A_3$ + metal - H]⁺ fragments from ion/ion reactions with fluoranthene at multiple reaction times using an isolation width of 0.5 m/z.

Fragment/Precursor	Theoretical D _{max} ^a	50 ms D _{max} ^b	100 ms D _{max} ^b	150 ms D _{max} ^b
$[^{1,4}X_2/A_3,^{0,3}X_2/A_3 + Ni - H]^+$	7.00/8.00	7.72 ± 0.01	7.69 ± 0.02	7.68 ± 0.02
$[^{1,4}X_2/A_3,^{0,3}X_2/A_3 + Mg - H]^+$	7.00/8.00	7.67 ± 0.02	7.62 ± 0.02	7.60 ± 0.02
$[^{1,4}X_2/A_3, ^{0,3}X_2/A_3 + \text{Co - H}]^+$	7.00/8.00	7.57 ± 0.02	7.53 ± 0.04	7.50 ± 0.05

^a Different theoretical D_{max} exist for isomeric fragments, which are listed based on the fragment order.

Differences between the experimental and theoretical D_{max} for different fragments adducted to the same metal (Table 2) suggest that structural differences effect HDX. It has been suggested that these differences in structure can be due to differences in how the metal-charge carrier is coordinated to the carbohydrate oxygens.⁶⁷ We ran MD simulations of ESI and optimized the resulting structures with DFT to determine probable coordination sites for each metal interacting with melezitose (Figures S4 – S7). The simulations suggest that metal coordination is similar for Ca^{2+} and Mg^{2+} with both metals preferring to bind in the "pocket" between all three monosaccharides in ~80 % of trials (Figure S4 – S5). Ni²⁺ and Co²⁺ show similar trends to each other with a smaller preference (~55 %) for binding in the "pocket" compared to Ca^{2+} and Mg^{2+} (Figure S6 – S7). The simulation data for Ca^{2+} and Mg^{2+} -adducted melezitose agrees with low-resolution ion-mobility (IM) data in that structures with similar gas-phase conformations were detected for Ca^{2+} - and Mg^{2+} -adducted melezitose.^{68, 69} Previous research has shown that electron transfer/proton transfer no dissociation (ET/PTnoD) followed by IM also impacts the collisional-cross

^b Data represents an average \pm standard deviation (n=12).

section of carbohydrates adducted to group II metals (Ca^{2+} and Mg^{2+}). However, low-resolution IM could not separate ET/PTnoD ([M + metal – H]⁺) products from precursors of melezitose adducted to either Ca^{2+} or Mg^{2+} , while HDX can distinguish Ca^{2+} - and Mg^{2+} -adducted fragments based on differences in D_{max} values, including the ET/PTnoD fragments (D_{max} values of (5.70 ± 0.03) D and (6.79 ± 0.06) D, respectively, Table S13). The work here suggests that the extent of HDX could be a complementary analysis method to other MS and IM techniques, with the extent of HDX being dependent on both the fragment structure and charge carrier.

Ion/ion reactions between protonated peptides and fluoranthene commonly yield charge-reduced fragments from ETD. ^{14, 16} Minimal HDX has been detected for these peptide fragments. Peptide fragments have been proposed to lose a hydrogen following ETD. ^{18, 60} Research by the Pagel and Brodbelt groups has predicted that deprotonated-carbohydrate ions have highly mobile deprotonation sites compared to deprotonated peptides. ^{70, 71} Based on previous *ab initio* MD simulations, the location of carbohydrate deprotonation delocalizes, causing rapid gas-phase charge migration on the ps timescale. The delocalization of the deprotonation site is due to a low energy barrier (<10 KJ/mol) for changing the location of the deprotonation site within carbohydrates.

Here, Ca²⁺- and Mg²⁺-adducted fragments were only detected with the loss of a hydrogen and exhibited more extensive HDX, while Ni²⁺- and Co²⁺-adducted fragments were detected with greater numbers of charge-reduced fragments and exhibited less extensive HDX (Figure 4 and Table S13). Thus, we hypothesize that charged-reduced fragments form more energetically stable fragments that can minimize HDX, while fragments with hydrogen loss have low energy barriers for charge migration, enabling greater amounts of HDX. Because the physical properties of the metal-charge carrier influence fragment formation, they also affect HDX. We hypothesize that higher charge-density metals (Mg²⁺, Co²⁺, and Ni²⁺) minimize HDX by minimizing charge migration. Furthermore, the second-ionization energy and electron configuration appear to be important metal properties because Ni²⁺, which has the highest second-ionization energy and a unique electron configuration (Table 1), minimizes HDX more than the

other metals examined here (Figure 3, Figure 4, Table 3, and Table S13). The higher second-ionization energy and electron configuration may help prevent the rapid migration of protons by increasing the energy barrier to HDX through charge localization and increased energetic stability.

d. HDX can occur during quadrupole isolation after collisional activation

Figure 4 and Table S13 show that D_{max} increased significantly at longer reaction times for Ni^{2+} - and Co^{2+} -adducted C_2/Y_2 and B_2/Z_2 fragments. Fragmentation can occur during quadrupole isolation (Figure 2), where collisional activation creates only doubly charged fragments ([fragment + metal]²⁺) and, singly charged fragments that lose a hydrogen ([fragment + metal - H]⁺). We determined that for some fragments, including the Co^{2+} -adducted C_2/Y_2 fragments, the average relative-intensity ratio of the charge-reduced fragments ($[C_2/Y_2 + Co]^+$) to the hydrogen-loss fragments ($[C_2/Y_2 + Co - H]^+$) increases with increasing ion/ion reaction time. For example, the ratio between the relative intensities of the charge reduced to hydrogen-loss C_2/Y_2 fragments was 0.06: 0.21 at 50 ms and 0.08: 0.23 at 100 ms (Table S14). The increase in the D_{max} at longer reaction times is unique to the Co^{2+} - and Ni^{2+} -adducted C_2/Y_2 fragments because charge-reduced fragments are not detected for the Mg^{2+} - and Ca^{2+} -adducted C_2/Y_2 fragments (Tables S1 -S4). As described above, we predict that charge-reduced fragments minimize HDX due to their energetic stability compared to hydrogen-loss fragments. Thus, as the ratio of charge-reduced fragments increases at longer reaction times, the D_{max} increases for Co^{2+} -adducted C_2/Y_2 fragments (Figure 4). This data suggests that the lower D_{max} at shorter reaction times may be related to the formation of hydrogen-loss fragments, such as those generated by quadrupole isolation before the ion/ion reaction.

We examined if HDX occurred in the quadrupole for Co^{2+} -adducted C_2/Y_2 fragments without the presence of fluoranthene by using HCD at 0% NCE (Figure 5). In Figure 5A, we see the undeuterated spectra, for Co^{2+} -adducted C_2/Y_2 fragments formed from quadrupole-isolation induced dissociation (isolation width of 0.5 m/z). The Co^{2+} -adducted C_2/Y_2 fragment was the only fragment we examined because the deuterated fragments adducted to Ni^{2+} , Mg^{2+} , and Ca^{2+} had signal intensities too low to examine after quadrupole-isolation induced activation. When examining deuterium-labeled melezitose,

only ~10-20% of the precursor ions are detected as fully deuterated due to back exchange that occurs in the instrument source, 45 reducing the signal intensity of each metal-adducted precursor ion. Furthermore, the fragments maintain different numbers of deuterium, dispersing the signal over multiple m/z values and further reducing the signal intensity for any particular m/z. Thus, only the Co^{2+} -adducted fragments had sufficient S/N for these analyses. For the Co^{2+} -adducted C_2/Y_2 fragments, we expected seven deuterium labels on the fragments that lose a hydrogen ($[C_2/Y_2 + Co - H]^+$). However, we detected between 0 D and 7 D with the most intense peak at 4 D (Figure 5B). Increasing the isolation width decreases fragment formation from quadrupole-isolation induced collisional activation (Tables S7, S9 – S12). Therefore, we evaluated if increasing the isolation width from 0.5 m/z to 20.0 m/z would affect HDX. In Figure 5C, we show that the D_{max} for the C_2/Y_2 fragment increases from (4.6 ± 0.2) D at an isolation width of 0.5 m/z to a D_{max} of (6.1 ± 0.2) D at an isolation width to minimize collisional activation, we can minimize fragment formation and HDX before the ion/ion reaction.

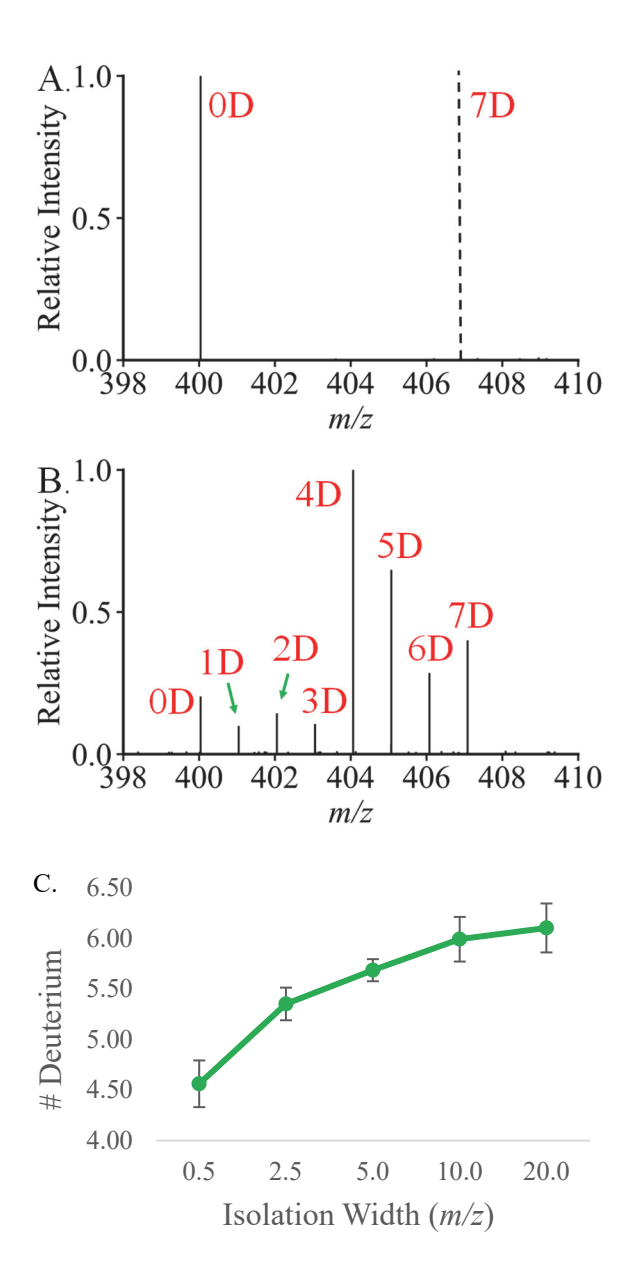


Figure 5. Representative spectra for the Co^{2^+} -adducted undeuterated (A, solid), predicted fully deuterated (A, dashed), and deuterated (B) C_2/Y_2 fragment at an isolation width of 0.5~m/z using HCD at 0% NCE. D represents the number of deuterium. (C) D_{max} values for the Co^{2^+} -adducted C_2/Y_2 fragment ([$\text{C}_2/\text{Y}_2 + \text{Co} - \text{H}]^+$) produced from HCD (0 % NCE) at different isolation widths. Data represents an average \pm standard deviation (n=12).

The increase in D_{max} values from using a larger quadrupole isolation width suggests that HDX occurs in the quadrupole and not in the ion routing multipole. This is significant because we can alter interactions

(collisions) within the quadrupole by altering the m/z isolation width, whereas ion interactions in the ion routing multipole are constant as ions are focused into either the linear-ion trap (LIT) for ion/ion reactions or the orbitrap for m/z detection.

Based on the decrease in HDX using wider quadrupole-isolation widths, we re-ran the ion/ion reaction experiments with fluoranthene using an isolation width of $10.0 \, m/z$ (Table S16). For the Co²⁺-adducted C₂/Y₂ fragments (Figure 6) and B₂/Z₂ fragments (Table S13, S16), we saw an increase in D_{max} when the isolation width was increased from $0.5 \, m/z$ to $10.0 \, m/z$ for a 50 ms reaction time. This suggests that using a larger isolation width can minimize HDX for fragments formed during quadrupole isolation to obtain higher D_{max} values for specific fragments at shorter reaction times.

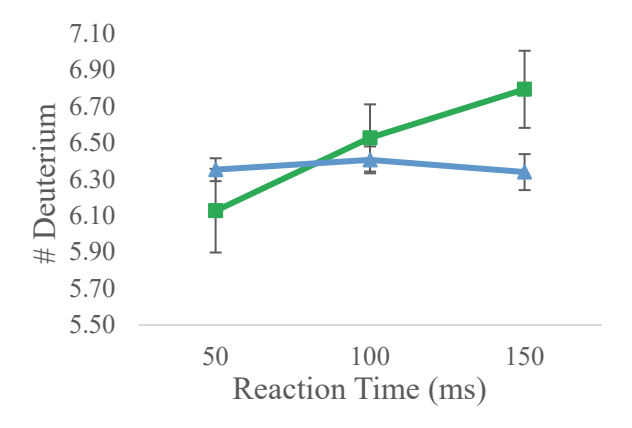


Figure 6. D_{max} values for Co^{2+} -adducted C_2/Y_2 fragments ($[C_2/Y_2 + C_0 - H]^+$, ($[C_2/Y_2 + C_0]^+$) from ion/ion reactions with fluoranthene at multiple reaction times with isolation widths of 0.5 m/z (green squares) or 10.0 m/z (blue triangles). Data represents an average \pm standard deviation (n=12).

We examined the deuterium distribution used for the corrected D_{max} calculations at an isolation width of $10.0 \, m/z$ to further quantify HDX occurring after the ion/ion dissociation reactions with fluoranthene. We focused on deuterium labeling distribution for the ET/PTnoD fragments (Figure 7) because these fragments were formed from ion/ion reactions and not from dissociation in the quadrupole (Figure 1 and Figure 2). The ET/PTnoD fragment was examined because we expect that, at most, one deuterium label

could be lost during the ion/ion reaction for ET/PTnoD fragments if no HDX occurs. For the ET/PTnoD fragments adducted to Ni^{2+} , we expected to detect the ET/PTnoD species with eight ([M + metal – H]⁺) or nine ([M + metal]⁺) deuterium (Figure 7B) if no HDX occurs because the precursor ion was detected with nine deuterium (Figure 7A). With Ni^{2+} -adducted ET/PTnoD fragments, we detected the most intense peak with seven deuterium (Figure 7B). For the Ca^{2+} -adducted ET/PTnoD fragments, we expected to detect nine deuterium labels on the ET/PTnoD fragment if no HDX occurs because the most intense precursor peak has 10 deuterium labels (Figure 7C). The data, however, shows that the most intense peak contains five deuterium (Figure 3D), indicating that the Ni^{2+} - and Ca^{2+} -adducted ET/PTnoD ions lose an average of two and four deuterium, respectively, during the 50 ms ion/ion reaction times. These deuterium distributions indicate that HDX occurs after ion/ion dissociation . Furthermore, Ca^{2+} -adducted fragments experience greater HDX than Ni^{2+} -adducted fragments, similar to C_2/Y_2 fragments (Figure 3). Yet, as the isolation width increases, it is more difficult to predict the number of deuterium labels on a fragment due to the heterogeneous population of isolated precursor ions with different numbers of deuterium labels, adding complexity to interpreting the data collected with isolation widths greater than $0.5 \, m/z$.

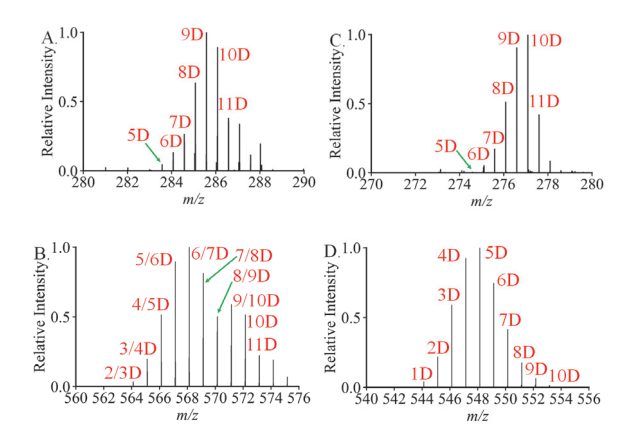


Figure 7. Representative spectra for the (A) Ni^{2^+} and (C) Ca^{2^+} -adducted, fully deuterated precursor and (B) Ni^{2^+} - and (D) Ca^{2^+} -adducted ET/PTnoD fragments after ion/ion reactions (50 ms). All isolation widths were $10.0 \, m/z$. D represents the number of deuterium in the fragments. For Ni^{2^+} , deuterium labels are the same as described in Figure 3. Unlabeled peaks in the spectra were not used for $\mathrm{D}_{\mathrm{max}}$ calculations due to the m/z values being outside the mass-error threshold.

The differences between D_{max} values in Tables S13 and Table S16 could result from multiple different sources. It has previously been hypothesized that primary hydroxyls exchange at a faster rate compared with secondary hydroxyls, ^{72, 73} yielding locations that retain or lose deuterium with higher probability before fragmentation, which could impact the corrected D_{max} values. When using an isolation width of 10.0 *m/z*, we are isolating and fragmenting a distribution of deuterated precursors that have between 5 and 11 deuterium (Figure 7A and 7C) compared to 11 deuterium on all precursors when using an isolation width of 0.5 *m/z* (Figure 3A and 3D). Therefore, differences in the corrected D_{max} could occur because we are isolating a distribution of deuterated species compared to the D_{max} values that come from only the fully deuterated species. This distribution of deuterated precursors likely impacts HDX because certain sites on the metal-adducted melezitose are more likely to remain deuterated after back-exchange during the ESI process. ⁴⁵ This source of error suggests that using a larger isolation width to examine deuterium labeling of ion/ion reactions may have some limitations.

We hypothesize that MS contaminants can cause HDX with fragments formed by either quadrupole isolation or ion/ion dissociation reactions. It is challenging to completely eliminate contaminants because the samples require storage containers that contain plasticizers and polymer additives⁷⁴ that could undergo HDX via ion/molecule reactions. HDX could also be due to collisions with background water or solvent (*e.g.*, methanol) vapor because the pressure in the quadrupole (~5.0x10⁻⁵ torr)⁷⁵ and the LIT (~5.0x10⁻⁵ torr) are unlikely to completely remove these vapors.

e. Fluoranthene is a source of HDX after the ion/ion dissociation reaction

 Co^{2+} - and Ni^{2+} -adducted fragments were formed at greater intensity than Ca^{2+} - and Mg^{2+} -adducted fragments during quadrupole isolation. Yet, more HDX was observed for Ca^{2+} -adducted fragments, compared to Co^{2+} - and Ni^{2+} -adducted fragments following ion/ion reactions (Figure 4). This suggests that Ca^{2+} -adducted fragments experience HDX due to interactions with fluoranthene. Fragments with a m/z > 425 are formed from interactions with fluoranthene, suggesting that HDX for these high m/z fragments can also be attributed to interactions with fluoranthene. Thus, only $\sim 25\%$ of the examined fragments would be affected by HDX prior to ion/ion reactions.

We ran additional experiments to determine if HDX was primarily occurring from interactions with fluoranthene or due to interactions with isolated contaminants or background water during the reaction time in the LIT. We accomplished this by examining the corrected D_{max} for the neutral hydrogen loss product, $[M + Co - H]^+$, (Table S17) because $[M + Co - H]^+$ can only be produced from either the ion/ion reaction or in-source CID, but not from collisional activation in the quadrupole (Tables S3, S7). Therefore, we can directly compare the change in corrected D_{max} values at different reaction times to determine if more HDX occurs when fluoranthene is present. Other metals were not examined due to the low intensity of the neutral-loss product produced from in-source CID. Here, we see that the corrected D_{max} value changes by 0.2 D when comparing a trapping/reaction time of 50 ms and 150 ms when the $[M + Co - H]^+$ fragments only interact with ionized contaminants, water, and/or solvent vapors (Table S17). However, with the introduction of fluoranthene, the corrected D_{max} changes by 0.59 D when comparing

reaction/trapping times of 50 ms and 150 ms (Table S16). Thus, the change in corrected D_{max} increases by \sim 300% when fluoranthene is present in the LIT. This data further suggests HDX occurs due to interactions between the fragment ions and fluoranthene.

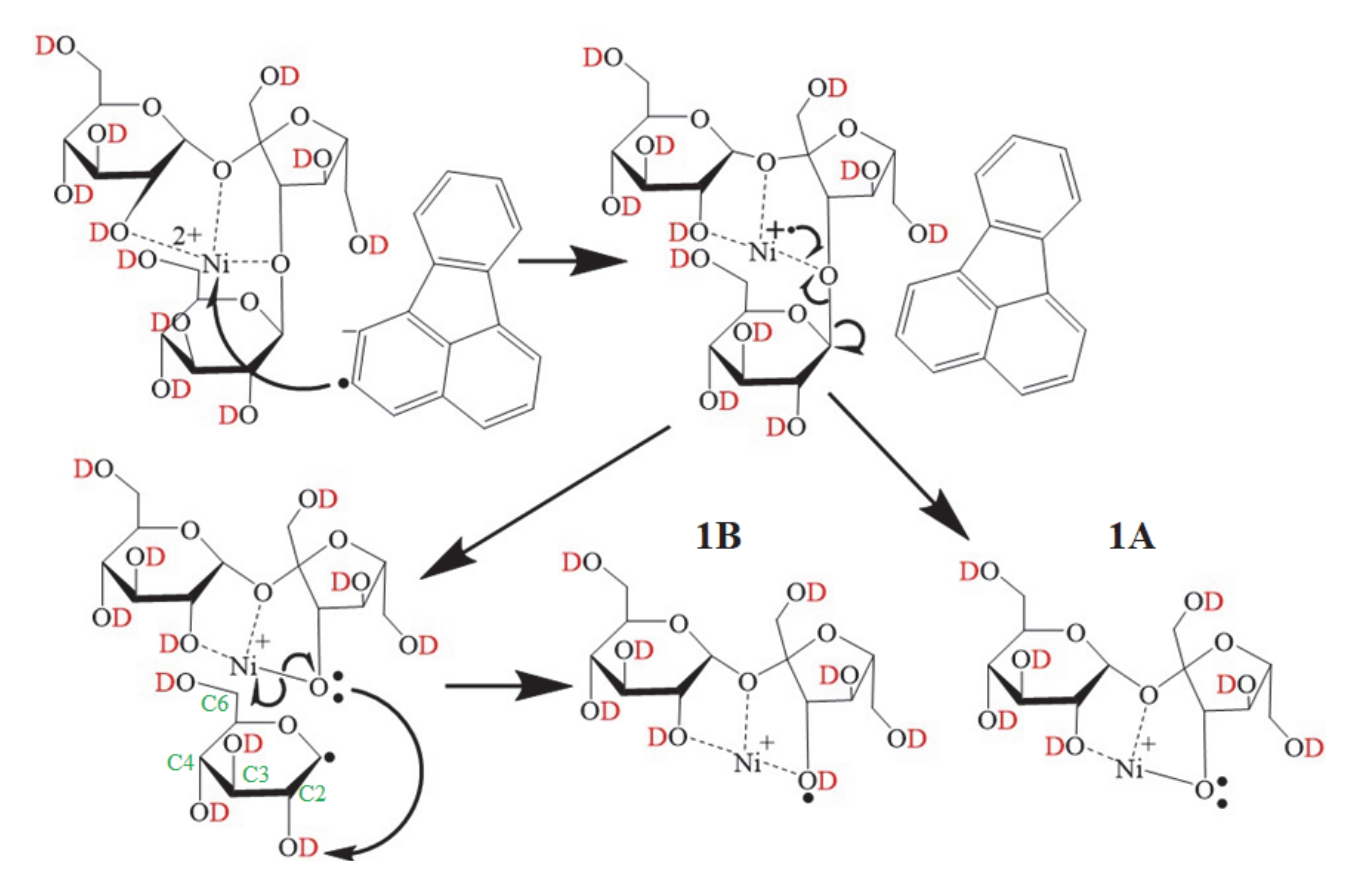
f. Proposed mechanisms of ETD, PTD, and intermolecular PT

Based on detection of [fragment + metal - H]⁺ with all metal-charge carriers, we propose that fragmentation for metal-adducted carbohydrates with fluoranthene can be initiated by either PT or ET. Ion/ion reactions between protonated peptides and anion reagents have shown that PT causes minimal dissociation; ¹⁸ however, ion/ion reactions with anionic glycosaminoglycans and cation reagents cause PT or ET followed by dissociation. ^{24,76} 7,8-Benzoquinoline, which has previously been reported to cause PTD of glycosaminoglycans, has a similar polyaromatic hydrocarbon structure to fluoranthene. Fragmentation by PTD has been associated with the proton affinity of the reagent. ²⁴ 7,8-Benzoquinoline (961 kJ/mol) has a lower proton affinity and causes more dissociation than 1,8-bis(dimethylamino)naphthalene (1028 kJ/mol). Fluoranthene has a lower proton affinity (829 kJ/mol)⁷⁷ than 7,8-benzoquinoline, which further suggests that PT from fluoranthene could cause dissociation of fragile ions, such as metal-adducted carbohydrates.

Proposed mechanisms for ETD and PTD of melezitose are shown in Schemes 1 and 2, respectively. As previously mentioned, MD simulations indicated that all four metals preferentially bind in the central "pocket" between the three monosaccharides within melezitose. Using the DFT optimized structures, we examined the distances between hydroxyl-H atoms and the glycosidic bonds within the precursor ions. Previously proposed ETD and ECD mechanisms have suggested that proton movement is important in initiating fragmentation, ^{61,65,78} with the most energetically favorable hydroxyl hydrogen being closest to the glycosidic bond. ⁷⁹ The modeling data suggested similar distances between hydroxyl-H atoms and the glycosidic bonds for all the metal adducts examined here (Tables S18 – S21). Therefore, we hypothesize that the chemical mechanisms for ETD, PTD, and intermolecular PT (or HDX) are independent of the

metal ion to produce a specific cleavage, though the metal-ion properties affect the likelihood of ETD, PTD, and HDX for a given fragment.

Scheme 1.



In ETD (Scheme 1), we hypothesize that an electron is initially accepted by the metal ion, which decreases the charge from +2 to +1. This aligns with ECD mechanisms in which the electron is first transferred to the metal. 58,65,80 Then, radical bond formation between a glycosidic-bond oxygen and the Ni⁺ radical is proposed to occur, followed by cleavage of the glycosidic bond to form a radical, neutral glucose and the $[C_2/Y_2 + Ni - H]^+$ fragment with hydrogen loss (1A). A deuterium can be abstracted from the neutral glucose to form the charge-reduced $[C_2/Y_2 + Ni]^+$ fragment (1B). Scheme 1 shows Ni²⁺ as the metal adduct because both the charge-reduced and hydrogen-loss $[C_2/Y_2 + Ni]^+/[C_2/Y_2 + Ni - H]^+$ fragments form (Figure 1B) with either eight or seven deuterium labels, respectively (Figure 3D). Based on the simulated structures for all four metal-adducts, we predict that the hydrogen in the carbon-2 hydroxyl is closest to the glycosidic bond at ~3.5 Å (Tables S18 – S21). All other hydrogens attached to

hydroxyls are \sim 1.5 Å farther from either glycosidic bond, making it unlikely for deuterium to be abstracted from those hydroxyls.

Scheme 2.

The proposed PTD mechanism for forming Ca²⁺-adducted C₂/Y₂ fragments is shown in Scheme 2. Fluoranthene initially abstracts a deuterium from a melezitose hydroxyl, shown here to be the carbon-2 hydroxyl, on the outer glucose. Then, the deprotonated oxygen attacks carbon-1, causing cleavage of the glycosidic bond. Formation of an anhydroglucose fragment has been proposed to occur in CID mechanisms for either deprotonated or Na⁺-adducted carbohydrates supporting the hypothesis that these fragments can form.^{81,82} It is also possible for a deuterium from another hydroxyl to be abstracted, and the

deprotonation site to shift to the carbon-2 hydroxyl before attacking the glycosidic bond. Scheme 2 shows Ca^{2+} as the metal adduct because only the $[C_2/Y_2 + Ca - H]^+$ fragments with hydrogen loss formed (Figure 1A) with seven deuterium labels (Figure 3B). The attack of carbon-1 by the carbon-2 oxygen is expected to be favored because the distance between the glycosidic bond and carbon-2 oxygen is ~1.5 Å shorter than the distances to the other oxygen atoms (Tables S18 – S21).

Scheme 3.

Based on the deuterium labeling data, we hypothesize that primarily fragments with the loss of a hydrogen ([Metal + fragment - H]⁺) undergo HDX through ion/molecule or ion/ion reactions after their initial dissociation reactions. The proposed mechanism for HDX with the Ca²⁺-adducted C₂/Y₂ fragment is shown in Scheme 3. Here, we show that a hydrogen-loss fragment formed from ETD (Scheme 1) or PTD (Scheme 2) can abstract a proton (labeled in blue) from nearby, neutral fluoranthene. In Scheme 3,

fluoranthene has a radical, which would indicate that PT initially occurred to form the neutral fluoranthene. However, if the neutral fluoranthene was formed from ET, a radical would not be present in Scheme 3. It is also possible that HDX could occur between carbohydrate-fragment cations and fluoranthene anion reagents that have not yet reacted. Although the deprotonated site is shown as the glycosidic oxygen in Scheme 3, the deprotonation site is likely rapidly migrating (on the order of ps) between oxygens with labile hydrogens/deuteriums. We postulate this delocalization of deprotonation could allow for rapid HDX reactions with fluoranthene by quickly shifting structures to form conformations where HDX is more energetically favorable.

4. Conclusions

Here, we have shown that deuterium labeling can effectively be used for mechanistic analyses of ion/ion reactions between metal-adducted carbohydrates and fluoranthene. Below is a list of key conclusions.

- The formation of charge-reduced fragments ([fragment + metal]⁺) from ion/ion reactions between carbohydrates and fluoranthene is dependent on the metal-charge carrier, with Co²⁺ and Ni²⁺ forming significant numbers of charge-reduced fragments.
- 2. Co²⁺ and Ni²⁺ form fragile ions when adducted to carbohydrates, which fragment during quadrupole isolation.
- 3. The extent of HDX following ion/ion dissociation reactions is related to the metal-charge carrier and the carbohydrate fragment structure.
- 4. Carbohydrate fragments formed in the quadrupole after ion activation can undergo HDX.
- 5. HDX is observed for metal-adducted carbohydrate fragments after the initial ion/ion dissociation reaction with fluoranthene, which is distinct from previous data examining protonated peptides.

Here, our data shows that HDX occurs for metal-adducted carbohydrate fragments, potentially due to interactions with fluoranthene, water vapor, solvent vapor, and/or other contaminants. Fluoranthene is

commonly used for ion/ion reactions that fragment metal-adducted carbohydrates. Therefore, future research could further explore the specific impact of fluoranthene in these HDX reactions. Regardless of the source, the existence of HDX indicates a fundamental mechanistic distinction between ion/ion reactions of carbohydrates with fluoranthene and other electron fragmentation methods, *e.g.*, electron capture dissociation (ECD).⁶¹ ECD is often considered to be analogous to ion/ion reactions with fluoranthene, but this data suggests that HDX is a product of ion/ion and/or ion/molecule reactions that can occur after the initial ion/ion dissociation reaction. These mechanistic experiments can provide insight into carbohydrate analysis via tandem MS and will enable further characterization of this important class of biomolecules.

5. Acknowledgments

This work was funded by the Welch Foundation (AA-1899) and the NSF (CHE-1945078). The authors thank the Baylor University Mass Spectrometry Center and the Baylor University Supercomputing Center for use of the high-performance computer cluster (Kodiak).

6. Supporting Information

Fragment identification lists (**Tables S1-S12**); Representative ion/ion-reaction spectra following deuterium labeling (**Figures S1-S3, S9-S10**); Average D_{max} values for fragments (**Tables S13, S15, S16, S17**); Proposed and representative DFT fragment structures (**Figure S3-S7**); Average relative intensity of Co²⁺-adducted C₂/Y₂ fragments (**Table S14**); Distances between hydroxyl H's on terminal Glc to glycosidic oxygen for metal-adducted melezitose (**Tables S18-21**)

- 1. Prentice, B. M.; McLuckey, S. A., Gas-phase ion/ion reactions of peptides and proteins: acid/base, redox, and covalent chemistries. *Chem Commun (Camb)* **2013**, *49* (10), 947-65.
- 2. Foreman, D. J.; McLuckey, S. A., Recent developments in gas-phase ion/ion reactions for analytical mass spectrometry. *Anal Chem* **2020**, *92* (1), 252-266.
- 3. Swaney, D. L.; McAlister, G. C.; Coon, J. J., Decision tree-driven tandem mass spectrometry for shotgun proteomics. *Nat Methods* **2008**, *5* (11), 959-64.
- 4. Riley, N. M.; Malaker, S. A.; Driessen, M. D.; Bertozzi, C. R., Optimal Dissociation Methods Differ for N- and O-Glycopeptides. *J Proteome Res* **2020**, *19* (8), 3286-3301.
- 5. Huguet, R.; Mullen, C.; Srzentic, K.; Greer, J. B.; Fellers, R. T.; Zabrouskov, V.; Syka, J. E. P.; Kelleher, N. L.; Fornelli, L., Proton Transfer Charge Reduction Enables High-Throughput Top-Down Analysis of Large Proteoforms. *Anal Chem* **2019**, *91* (24), 15732-15739.
- 6. Bailey, A. O.; Huguet, R.; Mullen, C.; Syka, J. E. P.; Russell, W. K., Ion-Ion Charge Reduction Addresses Multiple Challenges Common to Denaturing Intact Mass Analysis. *Anal Chem* **2022**.
- 7. Coon, J. J.; Ueberheide, B.; Syka, J. E. P.; Dryhurst, D. D.; Ausio, J.; Shabanowitz, J.; Hunt, D. F., Protein identification using sequential ion/ion reactions and tandem mass spectrometry. *PNAS* **2005**, *102*, 9463-9468.
- 8. Schaller-Duke, R. M.; Bogala, M. R.; Cassady, C. J., Electron transfer dissociation and collision-induced dissociation of underivatized metallated oligosaccharides. *J Am Soc Mass Spectrom* **2018**, *29* (5), 1021-1035.
- 9. Han, L.; Costello, C. E., Electron transfer dissociation of milk oligosaccharides. *J Am Soc Mass Spectrom* **2011,** *22* (6), 997-1013.
- 10. Syka, J. E. P.; Coon, J. J.; Schroeder, M. J.; Shabanowitz, J.; Hunt, D. F., Peptide and protein sequence analysis by electron transfer dissociation mass spectrometry. *PNAS* **2004**, *101* (26), 9528-9533.
- 11. McLafferty, F. W.; Schuddemage, H. D. R., Minimization of rearrangement reactions in mass spectra by use of collisional activation. *J Am Chem Soc* **1969**, *91* (7), 1866-1868.
- 12. Schroeder, M. J.; Webb, D. J.; Shabanowitz, J.; Horwitz, A. F.; Hunt, D. F., Methods for the Detection of Paxillin Post-translational Modifications and Interacting Proteins by Mass Spectrometry. *J Proteome Res* **2005**, *4* (5), 1832-1841.
- 13. Hogan, J. M.; Pitteri, S. J.; Chrisman, P. A.; McLuckey, S. A., Complementary Structural Information from a Tryptic N-Linked Glycopeptide via Electron Transfer Ion/Ion Reactions and Collision-Induced Dissociation. *J Proteome Res* **2005**, *4* (2), 628-632.
- 14. Zehl, M.; Rand, K. D.; Jensen, O. N.; Jørgensen, T. J. D., Electron Transfer Dissociation Facilitates the Measurement of Deuterium Incorporation into Selectively Labeled Peptides with Single Residue Resolution. *J Am Chem Soc* **2008**, *130* (51), 17453-17459.
- 15. Landgraf, R. R.; Chalmers, M. J.; Griffin, P. R., Automated hydrogen/deuterium exchange electron transfer dissociation high resolution mass spectrometry measured at single-amide resolution. *J Am Soc Mass Spectrom* **2012**, *23* (2), 301-9.
- 16. Rand, K. D.; Zehl, M.; Jensen, O. N.; Jørgensen, T. J. D., Protein Hydrogen Exchange Measured at Single-Residue Resolution by Electron Transfer Dissociation Mass Spectrometry. *Anal Chem* **2009**, *81* (14), 5577-5584.
- 17. Dongré, A. R.; Jones, J. L.; Somogyi, Á.; Wysocki, V. H., Influence of peptide composition, gas-phase basicity, and chemical modification on fragmentation efficiency: evidence for the mobile proton model. *J Am Chem Soc* **1996**, *118* (35), 8365-8374.
- 18. Gunawardena, H. P.; He, M.; Chrisman, P. A.; Pitteri, S. J.; Hogan, J. M.; Hodges, B. D. M.; McLuckey, S. A., Electron transfer versus proton transfer in gas-phase ion/ion reactions of polyprotonated peptides. *J Am Chem Soc* **2005**, *127* (36), 12627-12639.
- 19. Coon, J. J.; Syka, J. E. P.; Schwartz, J. C.; Shabanowitz, J.; Hunt, D. F., Anion dependence in the partitioning between proton and electron transfer in ion/ion reactions. *Int J Mass Spectrom* **2004**, *236* (1), 33-42.
- 20. Richardson, K.; Brown, J., In Silico Reagent Design for Electron-Transfer Dissociation on a Q-TOF. *J Am Soc Mass Spectrom* **2021**, *32* (8), 2092–2098.
- 21. Panepinto, M. C.; Duselis, E. M.; Shabanowitz, J.; Hunt, D. F., Nitrogen-Containing Aromatic Radical Anions Perform Multiple Proton and Electron Transfers Near-Simultaneously with Multiply Protonated Cations. *Anal Chem* **2021**, *93* (43), 14365-14368.

- 22. Sanders, J. D.; Mullen, C.; Watts, E.; Holden, D. D.; Syka, J. E. P.; Schwartz, J. C.; Brodbelt, J. S., Enhanced Sequence Coverage of Large Proteins by Combining Ultraviolet Photodissociation with Proton Transfer Reactions. *Anal Chem* **2020**, *92* (1), 1041-1049.
- 23. Stephenson, J. L.; McLuckey, S. A., Ion/ion proton transfer reactions for protein mixture analysis. *Anal Chem* **1996**, *68* (22), 4026-4032.
- 24. Bowers, J. J.; Hodges, B. D. M.; Saad, O. M.; Leary, J. A.; McLuckey, S. A., Proton hydrates as soft ion/ion proton transfer reagents for multiply deprotonated biomolecules. *Int J Mass Spectrom* **2008**, *276* (2), 153-159.
- 25. Herron, W. J.; Goeringer, D. E.; McLuckey, S. A., Gas-phase electron transfer reactions from multiply-charged anions to rare gas cations. *J Am Chem Soc* **1995**, *117* (46), 11555-11562.
- 26. Reily, C.; Stewart, T. J.; Renfrow, M. B.; Novak, J., Glycosylation in health and disease. *Nat Rev Nephrol* **2019**, 1.
- 27. Varki, A., Biological roles of glycans. *Glycobiology* **2017**, *27* (1), 3-49.
- 28. Schjoldager, K. T.; Narimatsu, Y.; Joshi, H. J.; Clausen, H., Global view of human protein glycosylation pathways and functions. *Nat Rev Mol Cell Biol* **2020**, *21* (12), 729-749.
- 29. Bode, L., Human milk oligosaccharides: every baby needs a sugar mama. *Glycobiology* **2012**, *22* (9), 1147-62.
- 30. Kobata, A., Structures and application of oligosaccharides in human milk. *Proc Jpn Acad, Ser B, Phys Biol Sci* **2010**, *86* (7), 731-747.
- 31. Bertozzi, C. R.; Rabuka, D., Structural basis of glycan diversity. In *Essentials of Glycobiology*, 2nd ed.; Varki, A.; Cummings, R. D.; Esko, J. D.; Freeze, H. H.; Stanley, P.; Bertozzi, C. R.; Hart, G. W.; Etzler, M. E., Eds. Cold Spring Harbor Laboratory Press: New York, 2009.
- 32. Kailemia, M. J.; Ruhaak, L. R.; Lebrilla, C. B.; Amster, I. J., Oligosaccharide analysis by mass spectrometry: a review of recent developments. *Anal Chem* **2014**, *86* (1), 196-212.
- 33. Ruhaak, L. R.; Xu, G.; Li, Q.; Goonatilleke, E.; Lebrilla, C. B., Mass Spectrometry Approaches to Glycomic and Glycoproteomic Analyses. *Chem Rev* **2018**, *118* (17), 7886-7930.
- 34. Grabarics, M.; Lettow, M.; Kirschbaum, C.; Greis, K.; Manz, C.; Pagel, K., Mass spectrometry-based techniques to elucidate the sugar code. *Chem Rev* **2021**, *122* (8), 7840-7908.
- 35. Gass, D. T.; Quintero, A. V.; Hatvany, J. B.; Gallagher, E. S., Metal adduction in mass spectrometric analyses of carbohydrates and glycoconjugates. *Mass Spectrom Rev* **2022**, e21801.
- 36. Harvey, D. J., Ionization and collision-induced fragmentation of N-linked and related carbohydrates using divalent cations. *J Am Soc Mass Spectrom* **2001**, *12* (8), 926-937.
- 37. Shannon, R. D., Revised effective ionic radii and systematic studies of interatomic distances in halides and chalcogenides. *Acta Crystallogr A* **1976**, *32* (5), 751-767.
- 38. Haynes, W. M.; Lide, D. R.; Bruno, T. J., *CRC handbook of chemistry and physics*. 97th ed.; CRC press: Boca Raton, FL, 2016.
- 39. Calixte, E. I.; Liyanage, O. T.; Kim, H. J.; Ziperman, E. D.; Pearson, A. J.; Gallagher, E. S., Release of carbohydrate-metal adducts from electrospray droplets: insight into glycan ionization by electrospray. *J Phys Chem B* **2020**, *124* (3), 479-486.
- 40. Harvey, D. J., Collision-induced fragmentation of underivatized *N*-linked carbohydrates ionized by electrospray. *J Mass Spectrom* **2000**, *35* (10), 1178-1190.
- 41. Calixte, E. I.; Liyanage, O. T.; Gass, D. T.; Gallagher, E. S., Formation of Carbohydrate-Metal Adducts from Solvent Mixtures during Electrospray: A Molecular Dynamics and ESI-MS Study. *J Am Soc Mass Spectrom* **2021,** *32* (12), 2738-2745.
- 42. Liyanage, O. T.; Brantley, M. R.; Calixte, E. I.; Solouki, T.; Shuford, K. L.; Gallagher, E. S., Characterization of electrospray ionization (ESI) parameters on in-ESI hydrogen/deuterium exchange of carbohydrate-metal ion adducts. *J Am Soc Mass Spectrom* **2019**, *30* (2), 235-247.
- 43. Senko, M. W.; Remes, P. M.; Canterbury, J. D.; Mathur, R.; Song, Q.; Eliuk, S. M.; Mullen, C.; Earley, L.; Hardman, M.; Blethrow, J. D.; Bui, H.; Specht, A.; Lange, O.; Denisov, E.; Makarov, A.; Horning, S.; Zabrouskov, V., Novel parallelized quadrupole/linear ion trap/Orbitrap tribrid mass spectrometer improving proteome coverage and peptide identification rates. *Anal Chem* **2013**, *85* (24), 11710-4.
- 44. Earley, L.; Anderson, L. C.; Bai, D. L.; Mullen, C.; Syka, J. E.; English, A. M.; Dunyach, J. J.; Stafford, G. C., Jr.; Shabanowitz, J.; Hunt, D. F.; Compton, P. D., Front-end electron transfer dissociation: a new ionization source. *Anal Chem* **2013**, *85* (17), 8385-90.

- 45. Kim, H. J.; Liyanage, O. T.; Mulenos, M. R.; Gallagher, E. S., Mass spectral detection of forward- and reverse-hydrogen/deuterium exchange resulting from residual solvent vapors in electrospray sources. *J Am Soc Mass Spectrom* **2018**, *29* (10), 2030-2040.
- 46. Compton, P. D.; Strukl, J. V.; Bai, D. L.; Shabanowitz, J.; Hunt, D. F., Optimization of electron transfer dissociation via informed selection of reagents and operating parameters. *Anal Chem* **2012**, *84* (3), 1781-5.
- 47. Domon, B.; Costello, C. E., A systematic nomenclature for carbohydrate fragmentations in FAB-MS/MS spectra of glycoconjugates. *Glycoconj J* **1988**, *5* (4), 397-409.
- 48. Ceroni, A.; Maass, K.; Geyer, H.; Geyer, R.; Dell, A.; Haslam, S. M., GlycoWorkbench: a tool for the computer-assisted annotation of mass spectra of glycans. *J Proteome Res* **2008**, *7* (4), 1650-1659.
- 49. Pan, J.; Borchers, C. H., Top-down mass spectrometry and hydrogen/deuterium exchange for comprehensive structural characterization of interferons: implications for biosimilars. *Proteomics* **2014**, *14* (10), 1249-58.
- 50. Group, W., GLYCAM Web. Complex Carbohydrate Research Center, University of Georgia, Athens, GA, 2005-2022.
- 51. Frisch, M. J.; Trucks, G. W.; Schlegel, H. B.; Scuseria, G. E.; Robb, M. A.; Cheeseman, J. R.; Scalmani, G.; Barone, V.; Petersson, G. A.; Nakatsuji, H.; Li, X.; Caricato, M.; Marenich, A. V.; Bloino, J.; Janesko, B. G.; Gomperts, R.; Mennucci, B.; Hratchian, H. P.; Ortiz, J. V.; Izmaylov, A. F.; Sonnenberg, J. L.; Williams; Ding, F.; Lipparini, F.; Egidi, F.; Goings, J.; Peng, B.; Petrone, A.; Henderson, T.; Ranasinghe, D.; Zakrzewski, V. G.; Gao, J.; Rega, N.; Zheng, G.; Liang, W.; Hada, M.; Ehara, M.; Toyota, K.; Fukuda, R.; Hasegawa, J.; Ishida, M.; Nakajima, T.; Honda, Y.; Kitao, O.; Nakai, H.; Vreven, T.; Throssell, K.; Montgomery Jr., J. A.; Peralta, J. E.; Ogliaro, F.; Bearpark, M. J.; Heyd, J. J.; Brothers, E. N.; Kudin, K. N.; Staroverov, V. N.; Keith, T. A.; Kobayashi, R.; Normand, J.; Raghavachari, K.; Rendell, A. P.; Burant, J. C.; Iyengar, S. S.; Tomasi, J.; Cossi, M.; Millam, J. M.; Klene, M.; Adamo, C.; Cammi, R.; Ochterski, J. W.; Martin, R. L.; Morokuma, K.; Farkas, O.; Foresman, J. B.; Fox, D. J. *Gaussian 16 Rev. C.01*, Wallingford, CT, 2016.
- 52. Hess, B.; Kutzner, C.; van der Spoel, D.; Lindahl, E., GROMACS 4: Algorithms for Highly Efficient, Load-Balanced, and Scalable Molecular Simulation. *J Chem Theory Comput* **2008**, *4* (3), 435-447.
- 53. Guvench, O.; Mallajosyula, S. S.; Raman, E. P.; Hatcher, E.; Vanommeslaeghe, K.; Foster, T. J.; Jamison, F. W., 2nd; Mackerell, A. D., Jr., CHARMM additive all-atom force field for carbohydrate derivatives and its utility in polysaccharide and carbohydrate-protein modeling. *J Chem Theory Comput* **2011**, *7* (10), 3162-3180.
- 54. Vanommeslaeghe, K.; Raman, E. P.; MacKerell, A. D., Jr., Automation of the CHARMM General Force Field (CGenFF) II: assignment of bonded parameters and partial atomic charges. *J Chem Inf Model* **2012**, *52* (12), 3155-68.
- 55. Konermann, L.; Metwally, H.; McAllister, R. G.; Popa, V., How to run molecular dynamics simulations on electrospray droplets and gas phase proteins: Basic guidelines and selected applications. *Methods* **2018**, *144*, 104-112.
- 56. McAllister, R. G.; Metwally, H.; Sun, Y.; Konermann, L., Release of Native-like Gaseous Proteins from Electrospray Droplets via the Charged Residue Mechanism: Insights from Molecular Dynamics Simulations. *J Am Chem Soc* **2015**, *137* (39), 12667-76.
- 57. Abascal, J. L. F.; Vega, C., A general purpose model for the condensed phases of water: TIP4P/2005. *J Chem Phys* **2005**, *123* (23), 234505.
- 58. Adamson, J. T.; Håkansson, K., Electron capture dissociation of oligosaccharides ionized with alkali, alkaline earth, and transition metals. *Anal Chem* **2007**, *79* (7), 2901-2910.
- 59. Liu, J.; McLuckey, S. A., Electron transfer dissociation: effects of cation charge state on product partitioning in ion/ion electron transfer to multiply protonated polypeptides. *Int J Mass Spectrom* **2012**, *330-332*, 174-181.
- 60. Mentinova, M.; Crizer, D. M.; Baba, T.; McGee, W. M.; Glish, G. L.; McLuckey, S. A., Cation recombination energy/coulomb repulsion effects in ETD/ECD as revealed by variation of charge per residue at fixed total charge. *J Am Soc Mass Spectrom* **2013**, *24* (11), 1676-89.
- 61. Zubarev, R. A.; Kelleher, N. L.; McLafferty, F. W., Electron capture dissociation of multiply charged protein cations. a nonergodic process. *J Am Chem Soc* **1998**, *120* (13), 3265-3266.

- 62. Wong, H. K.; Chen, X.; Wu, R.; Wong, Y. E.; Hung, Y. W.; Chan, T. D., Dissociation of mannose-rich glycans using collision-based and electron-based ion activation methods. *J Am Soc Mass Spectrom* **2022**, *33* (5), 803-812.
- 63. McClellan, J. E.; Murphy, J. P.; Mulholland, J. J.; Yost, R. A., Effects of Fragile Ions on Mass Resolution and on Isolation for Tandem Mass Spectrometry in the Quadrupole Ion Trap Mass Spectrometer. *Anal Chem* **2002**, *74* (2), 402-412.
- 64. Garrett, T. J.; Merves, M.; Yost, R. A., Characterization of protonated phospholipids as fragile ions in quadrupole ion trap mass spectrometry. *Int J Mass Spectrom* **2011**, *308* (2), 299-306.
- Huang, Y.; Pu, Y.; Yu, X.; Costello, C. E.; Lin, C., Mechanistic study on electron capture dissociation of the oligosaccharide-Mg²⁺ complex. *J Am Soc Mass Spectrom* **2014**, *25* (8), 1451-60.
- 66. Zhurov, K. O.; Fornelli, L.; Wodrich, M. D.; Laskay, U. A.; Tsybin, Y. O., Principles of electron capture and transfer dissociation mass spectrometry applied to peptide and protein structure analysis. *Chem Soc Rev* **2013**, *42* (12), 5014-30.
- 67. Rabus, J. M.; Pellegrinelli, R. P.; Khodr, A. H. A.; Bythell, B. J.; Rizzo, T. R.; Carrascosa, E., Unravelling the structures of sodiated β-cyclodextrin and its fragments. *Phys Chem Chem Phys* **2021**, *23* (24), 13714-13723.
- 68. Huang, Y.; Dodds, E. D., Discrimination of isomeric carbohydrates as the electron transfer products of group II cation adducts by ion mobility spectrometry and tandem mass spectrometry. *Anal Chem* **2015**, *87* (11), 5664-8.
- 69. Huang, Y.; Dodds, E. D., Ion-neutral collisional cross sections of carbohydrate isomers as divalent cation adducts and their electron transfer products. *Analyst* **2015**, *140* (20), 6912-21.
- 70. Struwe, W. B.; Baldauf, C.; Hofmann, J.; Rudd, P. M.; Pagel, K., Ion mobility separation of deprotonated oligosaccharide isomers evidence for gas-phase charge migration. *Chem Commun (Camb)* **2016**, *52* (83), 12353-12356.
- 71. Zhang, J.; Brodbelt, J. S., Gas-phase hydrogen/deuterium exchange and conformations of deprotonated flavonoids and gas-phase acidities of flavonoids. *J Am Chem Soc* **2004**, *126* (18), 5906-5919.
- 72. Kim, H. J. Rapid deuterium labeling and localization for structural elucidation of carbohydrates. Dissertation, Baylor University, 2021.
- 73. Bekiroglu, S.; Kenne, L.; Sandström, C., 1H NMR Studies of Maltose, Maltoheptaose, α -, β -, and γ -Cyclodextrins, and Complexes in Aqueous Solutions with Hydroxy Protons as Structural Probes. *J Org Chem* **2003**, *68* (5), 1671-1678.
- 74. Keller, B. O.; Sui, J.; Young, A. B.; Whittal, R. M., Interferences and contaminants encountered in modern mass spectrometry. *Anal Chim Acta* **2008**, *627* (1), 71-81.
- 75. Orbitrap Tribrid Series Hardware Manual. Revision A ed.; Thermo Fisher Scientific: 2018.
- 76. Wolff, J. J.; Leach, F. E.; Laremore, T. N.; Kaplan, D. A.; Easterling, M. L.; Linhardt, R. J.; Amster, I. J., Negative electron transfer dissociation of glycosaminoglycans. *Anal Chem* **2010**, *82* (9), 3460-3466.
- 77. Hunter, E. P. L.; Lias, S. G., Evaluated Gas Phase Basicities and Proton Affinities of Molecules: An Update. *J Phys Chem Ref* **1998**, *27* (3), 413-656.
- 78. Syrstad, E. A.; Turecček, F., Toward a general mechanism of electron capture dissociation. *J Am Soc Mass Spectrom* **2005**, *16* (2), 208-224.
- 79. Nguan, H. S.; Tsai, S. T.; Ni, C. K., Collision-Induced Dissociation of Cellobiose and Maltose. *J Phys Chem A* **2022**, *126* (9), 1486-1495.
- 80. Liu, H.; Håkansson, K., Divalent metal ion-peptide interactions probed by electron capture dissociation of trications. *J Am Soc Mass Spectrom* **2006**, *17* (12), 1731-1741.
- 81. Rabus, J. M.; Simmons, D. R.; Maitre, P.; Bythell, B. J., Deprotonated carbohydrate anion fragmentation chemistry: structural evidence from tandem mass spectrometry, infra-red spectroscopy, and theory. *Phys Chem Phys* **2018**, *20* (44), 27897-27909.
- 82. Rabus, J. M.; Abutokaikah, M. T.; Ross, R. T.; Bythell, B. J., Sodium-cationized carbohydrate gasphase fragmentation chemistry: influence of glycosidic linkage position. *Phys Chem Chem Phys* **2017**, *19* (37), 25643-25652.

